Evaluation of Noah Frozen Soil Parameterization for Application to a Tibetan Meadow Ecosystem

DONGHAI ZHENG, ROGIER VAN DER VELDE, AND ZHONGBO SU

Faculty of Geo-Information Science and Earth Observation, University of Twente, Enschede, Netherlands

JUN WEN AND XIN WANG

Key Laboratory of Land Surface Process and Climate Change in Cold and Arid Regions, Northwest Institute of Eco-Environment and Resources, Chinese Academy of Sciences, Lanzhou, China

KUN YANG

Department of Earth System Science, Tsinghua University, Beijing, China

(Manuscript received 18 August 2016, in final form 5 March 2017)

ABSTRACT

This study evaluates the Noah land surface model (LSM) in its ability to simulate water and heat exchanges over frozen ground in a Tibetan meadow ecosystem. A comprehensive dataset including in situ micrometeorological and soil moisture–temperature profile measurements collected between November and March is utilized, and analyses of the measurements reveal that the measured soil freezing characteristics are better captured by 1) modifying the parameter b_l implemented in the current Noah LSM that constrains the shape parameter of soil water retention curve utilized by the water potential freezing point depression equation to produce appropriate liquid water content $\theta_{\rm liq}$ under subzero temperature conditions and 2) neglecting the ice effect on soil-specific surface and thus matric potential via setting the empirical parameter that accounts for the effect of increase in specific surface of soil particles and ice–liquid water c_k to zero. The numerical experiments performed with the Noah model run show that in comparison to the default Noah LSM, adoption of $c_k = 0$ and site-specific b_l values reduces the overestimation of $\theta_{\rm liq}$ across the soil profile. Implementation of augmentations such as the parameterization of diurnally varying thermal roughness length resolves the overestimation of daytime turbulent heat fluxes and underestimation of surface temperature. Further adoption of a new heat conductivity parameterization reduces the overestimation of nighttime surface temperature. An appropriate treatment of phase change efficiency that accounts for changing freezing rate with varying liquid water contents is also needed to reduce the temperature underestimation across soil profiles.

1. Introduction

Frozen soils, including permafrost and seasonal frost, are widespread in high-latitude and high-altitude regions and cover more than half of the Northern Hemisphere during winters (Zhang et al. 1999, 2003). The coexistence of ice and liquid water in the frozen soil dramatically changes the soil hydraulic and thermal properties (Farouki 1986; Lawrence and Slater 2008; Lundin 1990) that in turn affects the water and heat distributions across the soil column as well as the exchanges with the overlying atmosphere (Hansson et al. 2004; Stevens et al. 2007; Zhao et al. 1997). The phase change of soil water, namely, freeze–thaw transition, also modulates the surface and subsurface energy partitioning that exerts a profound impact on the global and regional hydroclimatology (Lawrence et al. 2008; Poutou et al. 2004; Viterbo et al. 1999). An investigation of frozen soil processes is, therefore, imperative for global and regional climate change studies.

Accordingly, large efforts have been made recently to develop model physics for the effects of soil freeze–thaw process on water and energy budgets in land surface models (LSMs) and hydrological models (Cherkauer and Lettenmaier 1999; Dankers et al. 2011; Flerchinger and Saxton 1989; Gouttevin et al. 2012; Koren et al.

Corresponding author: Donghai Zheng, d.zheng@utwente.nl

DOI: 10.1175/JHM-D-16-0199.1

1999; Niu and Yang 2006). Current frozen soil parameterizations differ widely in the representation of model physics with respect to soil freeze–thaw processes; complexity of model structures and numerical schemes; and choice of governing equations, diagnostic variables, and model parameters (Li et al. 2010; Zhang et al. 2008, 2010). Large differences and discrepancies are found in the simulation of surface water and energy budgets generated by various models driven with the same meteorological forcing (Luo et al. 2003; Slater et al. 2007), for instance, the modeled hydrographs are often out of phase across the Arctic rivers. Further examinations of the model physics and validation against in situ measurements thus remain necessary.

The Tibetan Plateau is also in a substantial part underlain with permafrost and/or subject to seasonally frozen soil (Guo and Wang 2013), which makes the soil freeze–thaw process one of the key features for land surface modeling over the plateau. Recently, striking surface warming and frozen ground degradation have been widely reported (Salama et al. 2012; van der Velde et al. 2014; Wu and Zhang 2010; Wu et al. 2013), which altered the seasonal freeze–thaw cycle (Li et al. 2012) and exerted a profound influence on the local and surrounding hydrology and eco-environment (Cheng and Wu 2007; Jin et al. 2009; Wang et al. 2012). Better understanding and modeling of the frozen soil processes on the plateau is thus imperative because important sources of water and heat associated with freeze–thaw transitions are expected to be affected by climatic changes. In recent years, modeling of surface water and energy budgets on the Tibetan Plateau has been greatly advanced (Yang et al. 2009; Zheng et al. 2016, 2017), and current LSMs have been thoroughly investigated for a better simulation of soil water and temperature profiles (Chen et al. 2010; Zeng et al. 2012; Zheng et al. 2014, 2015c). Most of the studies are, however, mainly focused on thawed soil during the warm monsoon season, and fewer report on frozen soil (Cuo et al. 2015). Su et al. (2013) have recently shown that current LSMs have difficulty in capturing the freeze–thaw cycle on the Tibetan Plateau, and both heat and mass exchanges need to be accurately investigated to capture such process.

In this study, we seek to investigate and enhance the state-of-the-art Noah LSM in its ability to represent frozen soil processes in a Tibetan meadow ecosystem. The Noah LSM has been previously examined and modified to achieve a better simulation of water and heat flow in the thawed soil during the warm monsoon season from June to September (Zheng et al. 2015a,b). A comprehensive dataset including in situ micrometeorological and soil moisture–temperature profile measurements has been collected for the model assessment during the cold season between November and March.

This paper is outlined as follows. Section 2 introduces the Noah model physics and in situ measurements. Section 3 describes the diurnal variations of measured surface energy budgets as well as soil freezing characteristics. Section 4 provides a performance assessment of the Noah model physics associated with frozen soil processes. Section 5 presents a discussion on a performance assessment of alternative treatments of thermal heat conductivity as well as latent energy during water phase change. Section 6 concludes with a summary of the findings.

2. Methodology and measurements

a. Noah LSM frozen soil physics

The default Noah model physics as well as the augmentations associated with water and heat transport for unfrozen/thawed soil are described in detail in our previous studies (Zheng et al. 2015a,b). The model physics associated with frozen soil processes is given below.

To account for water phase change in frozen soil, a source–sink term is added to the thermal diffusion equation describing soil heat flow (Koren et al. 1999):

$$C_s(\theta,\theta_{\rm ice})\frac{\partial T_s}{\partial t}=\frac{\partial}{\partial z}\left[\kappa_h(\theta,\theta_{\rm ice})\frac{\partial T_s}{\partial z}\right]+I_{\rm lat} \quad \text{and} \quad (1a)$$

$$I_{\rm lat}=\rho_{\rm ice}L_f\frac{\partial\theta_{\rm ice}}{\partial t}, \quad (1b)$$

where T_s is the soil temperature (K), t is the time (s), z is the soil depth (m), $\rho_{\rm ice}$ is the density of ice (kg m^{-3}), L_f is the latent heat of fusion (J kg^{-1}), θ is the total soil water content (m^3 m^{-3}), $\theta_{\rm ice}$ is the soil ice content (m^3 m^{-3}), κ_h is the thermal heat conductivity (W m^{-1} K^{-1}), C_s is the thermal heat capacity (J m^{-3} K^{-1}), and $I_{\rm lat}$ represents the latent heat released or consumed during the phase change of soil water. Both κ_h and C_s depend on the constituents of the soil matrix (e.g., θ and $\theta_{\rm ice}$), and their parameterizations in Noah can be found in Peters-Lidard et al. (1998), whereby Zheng et al. (2015b) reported recently on the inclusion of the organic matter effect for the Tibetan soil.

The solution to Eq. (1) is achieved using the fully implicit Crank–Nicholson scheme. The temperature at the bottom boundary (at a depth of 8 m) is generally taken as the annual mean near-surface air temperature, whereas the top boundary is confined by the ground surface temperature $T_{\rm sfc}$ estimated by

$$T_{\rm sfc} = T_a + \frac{S^{\downarrow} - S^{\uparrow} + \varepsilon L^{\downarrow} - H - {\rm LE} - G_0}{4\varepsilon\sigma T_a^3} - \frac{1}{4}T_a, \quad (2)$$

where T_a is the air temperature (K); $S^{\downarrow}$ and $S^{\uparrow}$ are the downward and upward shortwave radiation ($\mathrm{W\,m^{-2}}$), respectively; $L^{\downarrow}$ is the downward longwave radiation ($\mathrm{W\,m^{-2}}$); ε is the surface emissivity (unitless); σ is the Stefan–Boltzmann constant taken as $5.67 \times 10^{-8}\,\mathrm{W\,m^{-2}\,K^{-4}}$; H is the sensible heat flux ($\mathrm{W\,m^{-2}}$); LE is the latent heat flux ($\mathrm{W\,m^{-2}}$); and G_0 is the ground surface heat flux ($\mathrm{W\,m^{-2}}$). Zheng et al. (2015b) reported recently several augmentations such as implementing the scheme of diurnally varying thermal roughness length for heat transfer z_{0h} to improve the surface heat flux and soil temperature simulations for thawed soil over Tibetan Plateau during warm season.

With the assumption that liquid water flow in the frozen soil is analogous to that in unfrozen/thawed soil, the diffusivity form of Richards' equation can be utilized to estimate unfrozen or liquid soil water movement (Koren et al. 1999):

$$\frac{\partial\theta_{\rm liq}}{\partial t} = \frac{\partial}{\partial z}\left[D(\theta_{\rm liq})\frac{\partial\theta_{\rm liq}}{\partial z}\right] + \frac{\partial K(\theta_{\rm liq})}{\partial z} + S(\theta), \quad (3)$$

where $\theta_{\rm liq}$ is the unfrozen/liquid soil water content ($\mathrm{m^3\,m^{-3}}$), D is the soil water diffusivity ($\mathrm{m^2\,s^{-1}}$), K is the hydraulic conductivity ($\mathrm{m\,s^{-1}}$), and S represents sources and sinks (i.e., infiltration and evapotranspiration; $\mathrm{m\,s^{-1}}$). Detailed descriptions of the default D, K, and S parameterizations are given in Chen et al. (1996), whereby Zheng et al. (2015a) included in Noah an asymptotic function for root water uptake and vertical heterogeneous soil hydraulic properties to enhance the description of water flow in thawed soil over Tibetan Plateau during warm season.

The heat source–sink term in Eq. (1) is determined by the soil water phase equilibrium estimated using the water potential freezing point depression equation as well as the available heat (Koren et al. 1999). The potential/equilibrium ice content is estimated as a function of both soil temperature and soil moisture content:

$$\frac{g\psi_s}{L_f}(1 + c_k\theta_{\rm ice})^2\left(\frac{\theta - \theta_{\rm ice}}{\theta_s}\right)^{-b} - \frac{T_s - T_f}{T_s} = 0, \quad (4)$$

where g is the acceleration of gravity ($\mathrm{m\,s^{-2}}$), c_k is an empirical parameter that accounts for the effect of increase in specific surface of soil particles and ice–liquid water (taken as 8.0), T_f is the freezing point temperature taken as 273.15 K, ψ_s is the soil water potential at air entry (m), θ_s is the porosity ($\mathrm{m^3\,m^{-3}}$), and b is an empirical parameter (unitless) related to the pore-size distribution of the soil matrix. The soil type–specific hydraulic parameters (i.e., θ_s, ψ_s, and b) are obtained from the class pedotransfer function (PTF) given in Cosby et al. (1984) augmented by Zheng et al. (2015a) to include the effect of organic matter as is typical for the Tibetan soil. Specifically, the effect of organic matter on the soil water retention curve (i.e., θ_s, ψ_s, and b) is considered via the additivity hypothesis, which estimates the hydraulic parameters as a weighted combination of mineral and organic fractions (Lawrence and Slater 2008; Zeiliguer et al. 2000) as

$$\theta_s = (1 - f_{t,\rm soc})\theta_{s,\rm min} + f_{t,\rm soc}\theta_{s,\rm soc}, \quad (5a)$$

$$\psi_s = (1 - f_{t,\rm soc})\psi_{s,\rm min} + f_{t,\rm soc}\psi_{s,\rm soc}, \quad \text{and} \quad (5b)$$

$$b = (1 - f_{t,\rm soc})b_{\rm min} + f_{t,\rm soc}b_{\rm soc}, \quad (5c)$$

where the $f_{t,\rm soc}$ is the volumetric soil organic fraction (unitless) and the hydraulic parameters of mineral soil (i.e., $\theta_{s,\rm min}$, $\psi_{s,\rm min}$, and $b_{\rm min}$) are obtained from the class PTF given in Cosby et al. (1984), while the hydraulic properties of pure organic matter (i.e., $\theta_{s,\rm soc}$, $\psi_{s,\rm soc}$, and $b_{\rm soc}$) are derived from Letts et al. (2000). According to Zheng et al. (2015a), the estimated b values are 7.35, 6.40, and 5.20 for depths of 5, 25, and 70 cm, respectively.

The Newton-type iteration is adopted for the solution of Eq. (4) with nonzero c_k values (i.e., $c_k > 0$):

$$\theta_{\rm ice}^{n+1} = \theta_{\rm ice}^{n} - \frac{f(\theta_{\rm ice}^{n})}{f'(\theta_{\rm ice}^{n})}, \quad (6a)$$

$$f(\theta_{\rm ice}^{n}) = \ln\left[\frac{g\psi_s}{L_f}(1 + c_k\theta_{\rm ice}^{n})^2\left(\frac{\theta^n - \theta_{\rm ice}^{n}}{\theta_s}\right)^{-b}\right] - \ln\left(-\frac{T_s^n - T_f}{T_s^n}\right), \quad \text{and} \quad (6b)$$

$$f'(\theta_{\rm ice}) = \frac{2c_k}{1 + c_k\theta_{\rm ice}^{n}} + \frac{b}{\theta^n - \theta_{\rm ice}^{n}}, \quad (6c)$$

where n represents the iterative step. The usage of natural logarithm in Eq. (6b) is to speed up the convergence of iteration.

Niu and Yang (2006) suggested to set the c_k value to zero, and the iteration is thus not needed for the solution of Eq. (4) with a zero c_k value (i.e., $c_k = 0$):

$$\theta_{\rm ice} = \theta - \theta_{{\rm liq},p} \quad \text{and} \quad (7a)$$

$$\theta_{{\rm liq},p} = \min\left[\theta, \theta_s\left(\frac{L_f}{g\psi_s}\frac{T_s - T_f}{T_s}\right)^{-1/b}\right], \quad (7b)$$

where $\theta_{{\rm liq},p}$ is the potential/equilibrium unfrozen/liquid soil moisture content ($\mathrm{m^3\,m^{-3}}$). Niu and Yang (2006) showed that Eq. (7) produces more soil ice content than

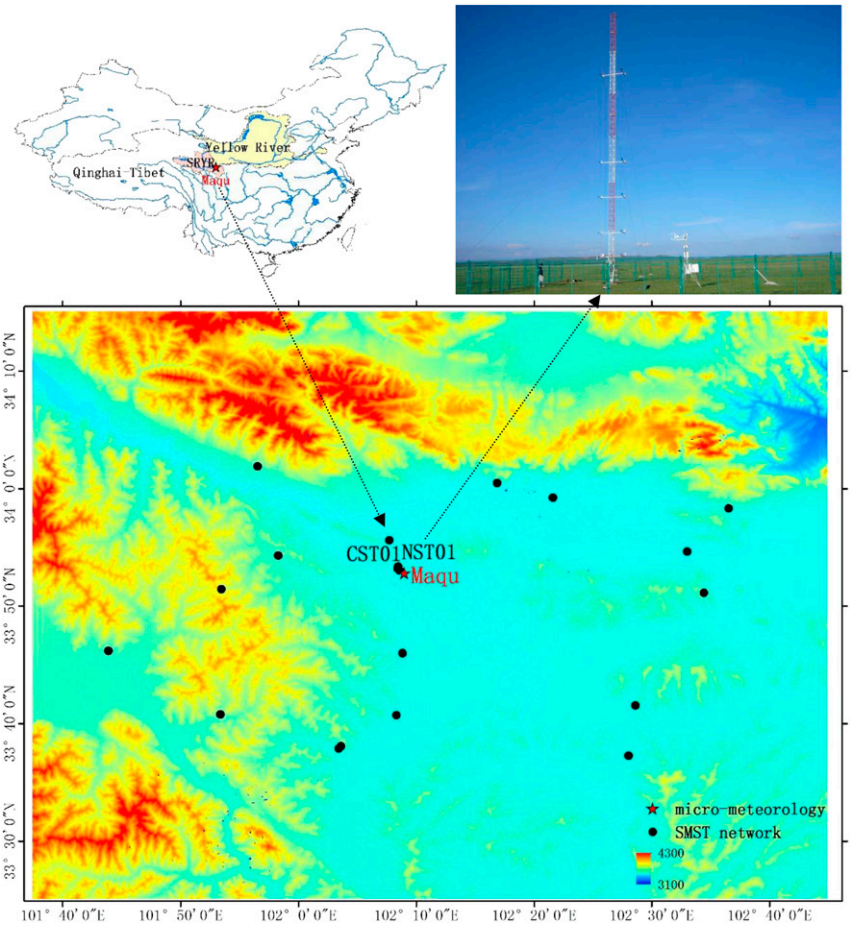

FIG. 1. (top left) Location of Maqu site in the SRYR in China, (top right) the micrometeorological station, and (bottom) the SMST monitoring network in the Maqu area shown on a DEM map.

does Eq. (6), and Bao et al. (2016) showed recently the validity of Eq. (7) for a Tibetan frozen soil site.

To avoid the simulation of unrealistically high values for the unfrozen/liquid soil water content at very low temperatures, a limit is set on parameter b in Eq. (4) and Eq. (6) [or Eq. (7)] when estimating ice content:

$$b = \min(b, b_l), \tag{8}$$

where b_l is an empirical parameter taken as 5.5.

b. *Field site and measurements*

The Maqu station is located in the source region of the Yellow River (SRYR) over the northeastern part of the Tibetan Plateau (Fig. 1), with elevations varying from 3100 to 4300 m above mean sea level. The weather is characterized by cold dry winters and rainy summers with soils that are generally frozen during cold season between November and April. Land cover in this region is dominated by alpine meadows with heights varying from 5 to 15 cm throughout the growing season. The prevailing soil types are silt loam, sandy loam, and organic soil (Dente et al. 2012; Zheng et al. 2015a).

The micrometeorological observing system at the Maqu station consisted of a 20-m planetary boundary layer (PBL) tower providing wind speed and direction, air temperature and humidity measurements at five heights above ground, and an eddy covariance (EC) system installed for measuring the turbulent heat fluxes. Instrumentations for measuring four radiation components (i.e., upward and downward shortwave and longwave radiation), air pressure, and precipitation are also deployed. A network of 20 soil moisture and soil temperature (SMST) monitoring sites is operational since 2008, of which two sites (CST01 and NST01) situated in the vicinity of the micrometeorological station are used for the analyses. The SMST profiles are automatically measured for depths of 5, 10, 20, 40, and 80 cm below the

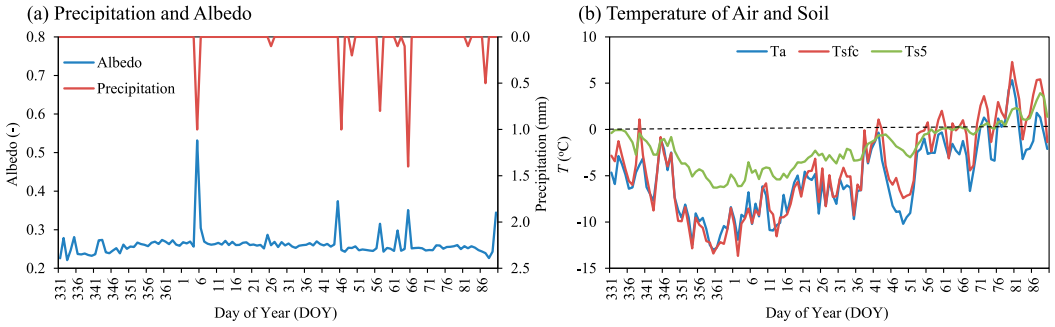

FIG. 2. Daily averaged (a) precipitation and albedo and (b) temperature of air, surface, and 5-cm soil depth for the period from 27 Nov 2009 (DOY 331) to 31 Mar 2010 (DOY 90).

soil surface using EC-TM ECH$_2$O probes (Decagon Devices, Inc., United States), and the root-mean-square error (RMSE) of soil moisture measurement is about 0.02 m^3 m^{-3} via a soil type–specific calibration according to Dente et al. (2012). In addition, soil samples were collected around the two SMST sites (CST01 and NST01) to quantify the soil properties via laboratory analyses, such as soil texture (sand, clay, and silt) and organic matter content. More details on the measurements and data processing can be found in Dente et al. (2012) and Zheng et al. (2015a).

The presented investigation spans the period from 27 November 2009 [day of year (DOY) 331] to 31 March 2010 (DOY 90), and all the data collected by the micrometeorological observing system and the two SMST sites during this period are reprocessed to values with a 30-min interval. Figure 2a shows the time series of daily averaged measured precipitation and albedo, whereby the albedo is calculated as the ratio of daily averaged measured upward and downward shortwave radiation. Figure 2b presents further the daily averaged measured temperatures of air (i.e., T_a), surface (i.e., T_{sfc}), and 5-cm soil depth T_{s5}. It can be noted that the daily averaged measured temperatures are generally below 0°C before DOY 71, and the presence of precipitation (snowfall) leads to the sharp increase of albedo indicating the presence of snowpack, which is generally short lived (less than 3 days for each duration).

3. Measured surface energy budgets and soil freezing at the Maqu site

a. Surface radiation and energy budgets

Figure 3a shows the mean diurnal variability for the period December–March of the measured surface radiation. Each component of the surface radiation increases from December to March, and the downward shortwave radiation (i.e., $S^{\downarrow}$) dominates the surface radiation budgets, with peak value varying from 600 W m^{-2} in December to 800 W m^{-2} in March. The peak values of the upward shortwave radiation (i.e., $S^{\uparrow}$) are around 140–190 W m^{-2}, and the surface albedo is on average about 0.23–0.24. The amplitude of the diurnal cycle of the downward longwave radiation (i.e., $L^{\downarrow}$) is much smaller compared to other radiation components, with an average value of 200 W m^{-2}. The values of the

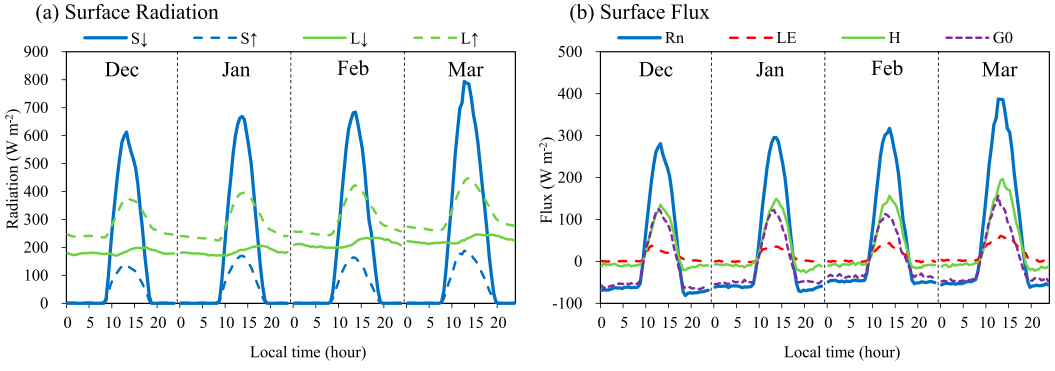

FIG. 3. Average diurnal cycles of December–March measured surface (a) radiation and (b) heat flux components.

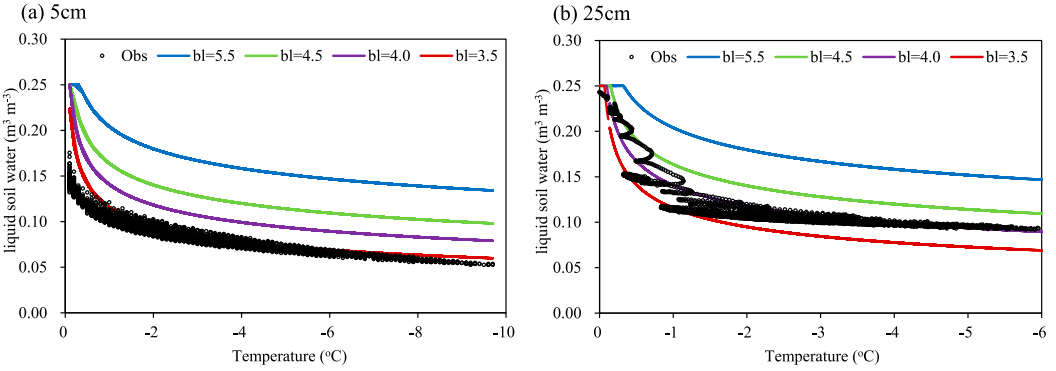

FIG. 4. Soil freezing characteristics determined from the measured and estimated liquid soil water vs measured soil temperature for depths of (a) 5 and (b) 25 cm.

upward longwave radiation $L^{\uparrow}$ generally increase from 250 W m^{-2} at night to 440 W m^{-2} at noon.

Figure 3b presents further the average diurnal cycle of the measured surface heat fluxes, within which the net radiation R_n is calculated as the sum of incoming and outgoing shortwave and longwave radiation, that is, $R_n = S^{\downarrow} + L^{\downarrow} - S^{\uparrow} - L^{\uparrow}$, and the ground heat flux (i.e., G_0) is estimated as the residual of surface energy balance, that is, $G_0 = R_n - H - \mathrm{LE}$. All surface heat fluxes also increase from December to March as a result of the R_n increase, and H is the main component of the surface energy budgets, with the peak value increasing from 135 W m^{-2} in December to 200 W m^{-2} in March. Negative values are generally found for G_0 at night, implying the heat loss from the soil column. Following with the sunrise and the warming due to the increase of solar radiation, the G_0 increases and reaches its maximum at noon, indicating the transport of heat into the soil column. The contribution of LE is much smaller because the freezing of liquid water constrains the evapotranspiration.

b. *Soil freezing characteristics*

Figures 4a and 4b show the soil freezing characteristics via plotting the measured soil temperatures with 30-min interval against corresponding measured or estimated liquid water contents for all subzero temperatures during the study period for soil depths of 5 and 25 cm, respectively. The estimated liquid soil water contents are derived via Eq. (7) with different settings of b_l values [see Eq. (8)], that is, 5.5, 4.5, 4.0, and 3.5. The usage of Eq. (7) with $c_k = 0$ instead of Eq. (6) is due to its numerical efficiency (Niu and Yang 2006), as has been previously applied to Tibetan frozen soils (Bao et al. 2016). The needed total soil water contents are estimated through linear interpolation between the liquid water contents measured before and after the freeze–thaw cycle as in Flerchinger et al. (2006).

As shown in Fig. 4, the estimated liquid water contents with the default b_l value (i.e., $b_l = 5.5$) adopted by current Noah LSM largely overestimate the measurements for all subzero temperatures, indicating that the default b_l value is not suitable for applications to Tibetan frozen soils, and site or soil type–specific values are preferable. It can be also found from Fig. 4 that smaller b_l values are more suitable, for instance, the estimated liquid water contents with $b_l = 3.5$ and $b_l = 4.0$ best capture the measurements for soil depths of 5 and 25 cm, respectively.

4. Assessment of Noah frozen soil parameterization

a. *Experimental design*

Three experiments are designed to assess the performance of Noah frozen soil parameterization with default settings and augmentations (section 2a) as well as site-specific values (section 3b). A control experiment (Ctrl) is performed first by running the Noah LSM with its default model physics. The second experiment (EXP1) contains a Noah model run with the implementation of the augmentations, including a diurnally varying roughness length for heat transfer (i.e., z_{0h}), an asymptotic function for root water uptake, and vertical heterogeneous soil thermal and hydraulic properties all modified to better represent the Tibetan environment (Zheng et al. 2015a,b). For the third experiment (EXP2), Eq. (6) is further replaced with Eq. (7) with $c_k = 0$ because of its numerical efficiency and suitability for Tibetan frozen soil (Bao et al. 2016; Niu and Yang 2006), and the site-specific b_l values given in section 3b are also implemented, while other settings are identical to EXP1. Specifically, the value of b_l is specified as 3.5 for the first soil layer, and a value of 4.0 is assigned for other soil layers.

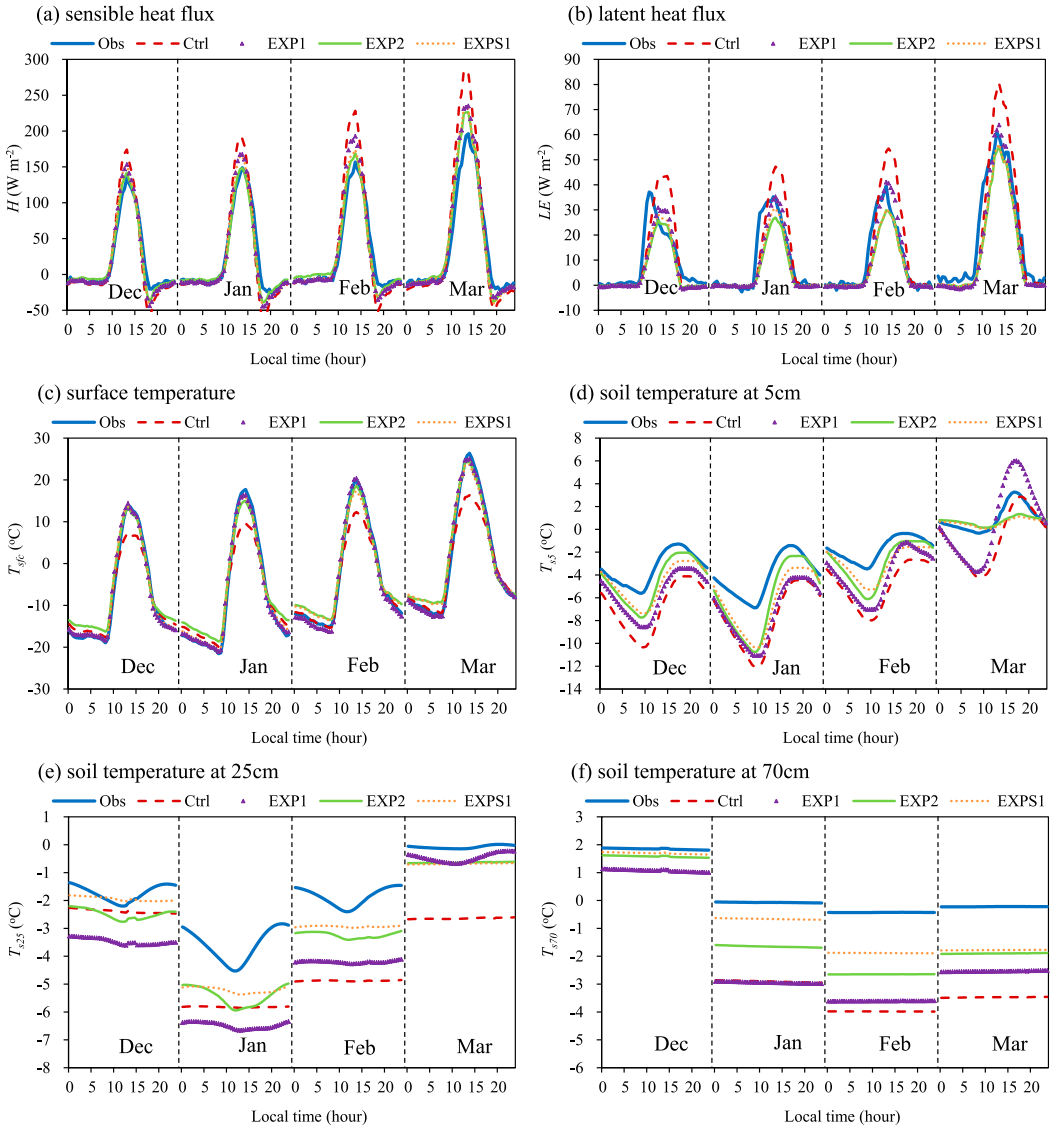

FIG. 5. Average diurnal cycles of December–March measured and simulated (a) sensible heat flux, (b) latent heat flux, (c) surface temperature, and soil temperature for the depths (d) 5, (e) 25, and (f) 70 cm produced by four numerical experiments performed in sections 4 and 5a.

All the numerical experiments are forced by the micrometeorological measurements collected from 27 November 2009 to 31 March 2010 at the Maqu site (section 2b), which includes downward and upward shortwave radiation, downward longwave radiation, wind speed, air temperature, relative humidity, air pressure, and precipitation. The prescribed vegetation and soil types are grassland and silt loam, respectively, and the adopted vegetation and soil parameters are identical to simulations reported in Zheng et al. (2015a). Soil moisture and temperature measurements are used to initialize each model run as well as to validate Noah simulations. For both, the measurements collected at sites CST01 and NST01 are averaged for each soil depth (e.g., 0.05, 0.10, 0.20, 0.40, and 0.80 m), and interpolated to the midpoints of the upper three model layers (i.e., 0.05, 0.25, and 0.70 m). Then, the soil moisture and temperature of the fourth layer is taken for initialization equal to the states of the third layer. The Noah simulations are validated further through comparisons of the simulated turbulent heat fluxes with measurements collected by an EC system.

b. *Turbulent heat flux and soil state simulations*

Figure 5 shows the mean diurnal cycle for December–March of the measured and simulated turbulent heat

TABLE 1. RMSE computed between the measured and simulated sensible and latent heat fluxes and surface and soil temperature at depths of 5, 25, and 70 cm produced by all the numerical experiments with a 30-min interval for the period from 27 Nov 2009 to 31 Mar 2010.

RMSE	H (W m^{-2})	LE (W m^{-2})	T_{sfc} (K)	T_{s5} (K)	T_{s25} (K)	T_{s70} (K)
Ctrl	37.74	14.18	4.06	3.68	2.33	2.79
EXP1	24.12	11.80	2.19	2.98	2.18	2.45
EXP2	22.52	12.07	3.11	1.97	1.39	1.61
EXPS1	23.08	11.79	2.47	2.08	1.21	1.13
EXPS2	23.90	11.87	2.30	2.33	1.19	0.76
EXPS3	23.20	11.81	2.38	1.98	1.27	1.04
EXPS4	23.67	11.78	2.59	1.03	0.57	0.72

fluxes (H and LE) and soil temperature profiles, and Table 1 provides the corresponding RMSE computed between all the measurements and simulations with a 30-min interval for the period between 27 November 2009 (DOY 331) and 31 March 2010 (DOY 90). Figure 6 further presents the time series of the measured and simulated liquid soil water profiles with a 30-min interval, and the corresponding RMSEs are listed in Table 2. Analysis of the measured liquid soil water profiles (Fig. 6) reveals that soil water in the first layer (i.e., 5 cm) starts freezing at the beginning of study period (27 November 2009, DOY 331), and the freezing front reaches its maximum around mid-February 2010 (DOY 41). The soil ice in the first layer starts thawing at the end of February (DOY 51) and is almost totally thawed out at the end of study period (31 March 2010, DOY 90). The dates of freezing and thawing are reached at a later time for greater soil depths, for instance, the soil water in the second layer (i.e., 25 cm) starts freezing at about one week later than that of first layer.

In its default model configuration, Noah (Ctrl) largely overestimates the daytime turbulent heat fluxes (Figs. 5a,b) and underestimates the surface temperature (Fig. 5c), which is greatly ameliorated by the EXP1 with the implementation of the augmentations such as the scheme of diurnally varying thermal roughness length for heat transfer (i.e., z_{0h}). Identical results and explanations have been reported for the thawed soil in the Maqu site during the warm monsoon season as in Zheng et al. (2015b). In comparison to the Ctrl, the EXP1 reduces the RMSE computed between the measured and simulated H, LE, and T_{sfc} by about 36%, 17%, and 46%, respectively.

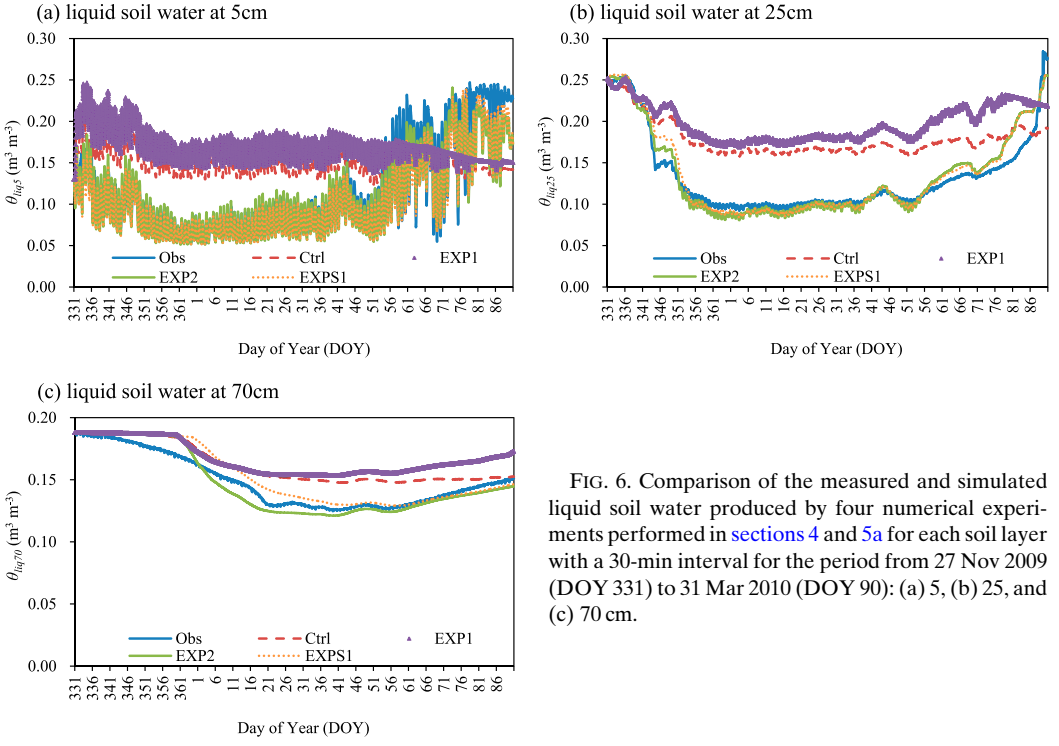

FIG. 6. Comparison of the measured and simulated liquid soil water produced by four numerical experiments performed in sections 4 and 5a for each soil layer with a 30-min interval for the period from 27 Nov 2009 (DOY 331) to 31 Mar 2010 (DOY 90): (a) 5, (b) 25, and (c) 70 cm.

TABLE 2. RMSE computed between the measured and simulated liquid soil water at depths of 5 cm θ_{liq5}, 25 cm θ_{liq25}, and 70 cm (i.e., θ_{liq70}) produced by all the numerical experiments with a 30-min interval for the period from 27 Nov 2009 to 31 Mar 2010.

RMSE	θ_{liq5} ($m^3\,m^{-3}$)	θ_{liq25} ($m^3\,m^{-3}$)	θ_{liq70} ($m^3\,m^{-3}$)
Ctrl	0.065	0.054	0.015
EXP1	0.076	0.072	0.020
EXP2	0.020	0.013	0.007
EXPS1	0.022	0.014	0.008
EXPS2	0.027	0.028	0.012
EXPS3	0.018	0.015	0.010
EXPS4	0.020	0.014	0.016

Similar to the findings reported in section 3b, both Ctrl and EXP1 with the default b_l value largely overestimate the liquid water contents (i.e., θ_{liq}) in the soil profile (Fig. 6). Consequently, less latent heat [i.e., I_{lat}; Eq. (1)] is released or consumed during the phase change of soil water, which explains the underestimations found for the temperature in the soil profile as seen in Figs. 5d–f.

Notably, the θ_{liq} overestimations by both Ctrl and EXP1 are significantly reduced within the EXP2 (Fig. 6) via the implementation of $c_k = 0$ as well as site-specific b_l values, because the measured θ_{liq} for depths of 5 and 25 cm during the study period are used to derive the site-specific b_l values (section 3b). The EXP2 is able to capture much better the measured θ_{liq} dynamics in the soil profile, which reduces the RMSE in comparison to the Ctrl computed between the measured and simulated θ_{liq} for depths of 5, 25, and 70 cm by about 69%, 76%, and 53%, respectively. Also, improvements are noted for the simulation of soil temperature (Figs. 5d–f) because of better simulation of soil freeze–thaw transition (i.e., θ_{liq} dynamics), and thus I_{lat}, with RMSE reduced by about 46%, 40%, and 42% for depths of 5, 25, and 70 cm, respectively. In comparison to EXP1, EXP2 produces less liquid water (Fig. 6a) and more ice content for the surface layer that increases the surface heat conductivity. This leads to the increase in the amplitude of the diurnal ground heat flux variation and thus the decrease in the amplitude of the diurnal surface temperature [see Eq. (2), Fig. 5c] and turbulent heat flux (Figs. 5a,b) variations. It can be found that the EXP2 overestimates the nighttime surface temperature and underestimates the temperature across the soil profile (Figs. 5d–f), which will be further investigated in the following section.

5. Discussion

a. Thermal heat conductivity

1) PARAMETERIZATION

The overestimation of nighttime surface temperature as noted in section 4 by the EXP2 may be caused by the overestimation of thermal heat conductivity in the soil. The κ_h parameterization currently adopted by the Noah LSM (see section 2a) has recently been modified to represent the Tibetan frozen soil conditions by Bao et al. (2016):

$$\kappa_h = \kappa_{dry} + \kappa_{wet} + \kappa_{ice}\theta_{ice}, \tag{9a}$$

$$\kappa_{dry} = \frac{0.135\rho_b + 64.7}{2700 - 0.947\rho_b}, \tag{9b}$$

$$\kappa_{wet} = (\kappa_{sat} - \kappa_{dry})\exp[0.36(1 - \theta_s/\theta_{liq})], \quad \text{and} \tag{9c}$$

$$\kappa_{sat} = (\kappa_{qtz}^{qtz}\kappa_o^{1-qtz})^{1-\theta_s}\kappa_w^{\theta_s}, \tag{9d}$$

where κ_{dry}, κ_{wet}, and κ_{sat} are the heat conductivity of dry, wet, and saturated soil ($W\,m^{-1}\,K^{-1}$), respectively; κ_{ice} is the heat conductivity of ice (taken as $2.2\,W\,m^{-1}\,K^{-1}$); κ_w is the heat conductivity of water (taken as $0.57\,W\,m^{-1}\,K^{-1}$); κ_{qtz} is the heat conductivity of quartz (taken as $7.7\,W\,m^{-1}\,K^{-1}$); κ_o is the heat conductivity of other soil particles (taken as $2.0\,W\,m^{-1}\,K^{-1}$); qtz is the volumetric quartz fraction (unitless); and ρ_b is the bulk density of dry soil ($kg\,m^{-3}$).

2) SURFACE HEAT FLUX AND SOIL STATE SIMULATIONS

An additional numerical experiment (EXPS1) is carried out to assess the sensitivity of model results when the default κ_h parameterization is replaced with the one by Bao et al. (2016) [Eqs. (9a)–(9d)], whereby other settings are taken as in EXP2. The average diurnal turbulent heat flux and soil temperature cycle as well as the time series of liquid soil water dynamics produced by EXPS1 are added to Figs. 5 and 6, respectively. The corresponding error statistics are added to Tables 1 and 2 as well.

Notably, the overestimation of nighttime surface temperature is resolved with the implementation of new κ_h parameterization (Fig. 5c) that reduces the heat conductivity and thus ground heat flux, and the underestimation of the temperature in the deeper soil layers (e.g., soil temperature at 70-cm depth T_{s70}; Fig. 5f) is largely reduced because less heat is released from the soil column. In comparison to EXP2, this reduces the RMSE computed between the measured and simulated surface temperature, soil temperature at 25-cm depth T_{s25}, and soil temperature at 70-cm depth by about 21%, 13%, and 30%, respectively (Table 1). The EXPS1-simulated liquid soil water dynamics are comparable to those produced by the EXP2 (Fig. 6, Table 2), while more liquid water is generated for deeper layers (e.g., liquid soil water at 70-cm depth θ_{liq70}; Fig. 5f) as the temperature is higher [see Eq. (7b)]. It should be noted

that the EXPS1 does not resolve the deficiency in simulating T_{s5} (Fig. 5d), which will be addressed in the following section.

b. Latent heat of fusion

1) PARAMETERIZATIONS

The underestimation of soil temperature profiles as noted in sections 4 and 5a may be related to the poor simulation of latent heat (i.e., $I_{\rm lat}$) released or consumed during the phase change of soil water. In the Noah LSM, $I_{\rm lat}$ is represented as a source–sink term in the thermal diffusion equation [see Eq. (1)], whereby the whole equation is solved using the fully implicit Crank–Nicholson scheme. In other LSMs, there is an alternative numerical algorithm within which the $I_{\rm lat}$ is ignored at first while solving the thermal diffusion equation, then the phase change is evaluated, and the soil temperature as well as the ratio of liquid water and ice contents is readjusted by energy conservation during the phase change. Such treatment of $I_{\rm lat}$ is commonly employed in LSMs, such as Noah-MP (Niu et al. 2011); Community Land Model (CLM; Oleson et al. 2013); Interactions between Soil, Biosphere, and Atmosphere (ISBA) model (Decharme et al. 2011; Masson et al. 2013); and a modified Simple Biosphere Model (Bao et al. 2016) because of its numerical efficiency. For instance, the treatment of $I_{\rm lat}$ in Noah-MP (Niu et al. 2011) is as follows:

$$\begin{matrix} T_s^{n+1} > T_f \quad \text{and} \quad \theta_{\rm ice}^n > 0 \text{ melting} \\ T_s^{n+1} < T_f \quad \text{and} \quad \theta_{\rm liq}^n > \theta_{{\rm liq},p} \text{ freezing} \end{matrix}, \tag{10a}$$

$$\theta_{\rm ice}^{n+1} = \begin{cases} \max(\theta_{\rm ice}^n - H_m, 0), & H_m > 0 \\ \min(\theta_{\rm ice}^n - H_m, \theta^n - \theta_{{\rm liq},p}), & H_m < 0 \end{cases}, \tag{10b}$$

$$\theta_{\rm liq}^{n+1} = \max(\theta^n - \theta_{\rm ice}^{n+1}, 0), \tag{10c}$$

$$H_m = \frac{T_s^{n+1} - T_f}{L_f} \frac{C_s}{1000}, \quad \text{and} \tag{10d}$$

$$T_s^{n+1} = T_s^{n+1} - \frac{L_f(\theta_{\rm ice}^n - \theta_{\rm ice}^{n+1})1000}{C_s}, \tag{10e}$$

where n represents the time step, T_f is the freezing point temperature specified as 273.15 K, $\theta_{{\rm liq},p}$ is the potential/maximum liquid soil water content estimated using Eq. (7b), and H_m represents the excess or deficit of energy during phase change of soil water.

In reality, the freezing point temperature should not be a constant, which can be alternatively estimated using the Gibbs free-energy concept as (Masson et al. 2013; Zhang et al. 2007)

$$T_f = \frac{L_f(273.15)}{L_f - g\left[\psi_s\left(\frac{\theta_{\rm liq}}{\theta_s}\right)^{-b}\right]}. \tag{11}$$

In addition, a parameter ε that represents the phase change efficiency can be introduced into Eq. (10d), which is similar to the method used in the ISBA model (Masson et al. 2013):

$$H_m = \varepsilon \frac{T_s^{n+1} - T_f}{L_f} \frac{C_s}{1000} \quad \text{and} \tag{12a}$$

$$\varepsilon = \begin{cases} 2.0\theta_{\rm liq}/\theta, & T_s^{n+1} < T_f \\ 1.0, & T_s^{n+1} > T_f \end{cases}. \tag{12b}$$

The above equations assume that the freezing rate (release of latent energy) increases when less liquid water content is present in the soil. It should be also noted that the parameterization of ε is derived empirically via the trial and error method through comparison of the simulations with corresponding measurements.

2) IMPACT ON SURFACE HEAT FLUX AND SOIL STATE SIMULATIONS

To investigate the performance of these aforementioned alternative treatments of $I_{\rm lat}$ for their abilities to simulate the soil temperature profiles, three additional numerical experiments are carried out. For the first experiment (EXPS2), the default parameterization of $I_{\rm lat}$ in the Noah LSM [Eq. (1)] is replaced by the alternative algorithm as described by Eqs. (10a)–(10e), while other settings are taken from EXPS1. In the second experiment (EXPS3), Noah is run with the same options as EXPS2 but the freezing point temperature is calculated by Eq. (11) instead of using the constant value 273.15 K. The parameter ε representing the phase change efficiency as described in Eqs. (12a) and (12b) is included in the third experiment (EXPS4), and other settings are identical to EXPS3.

The RMSE statistics computed between the measured and simulated turbulent heat fluxes and soil temperature produced by the three additional numerical experiments are listed in Table 1. It shows that all the three additional experiments produce comparable results for turbulent heat fluxes and surface temperature as the EXP2 and EXPS1, indicating that the implementation of these alternative treatments of $I_{\rm lat}$ has minor impact on the simulated land–atmosphere exchanges of heat and mass that are mostly controlled by the parameterization of the diurnally varying roughness length for heat transfer (section 4). In support of further analyses, Fig. 7 presents the mean diurnal variability of the measured and simulated surface temperature and soil temperature for

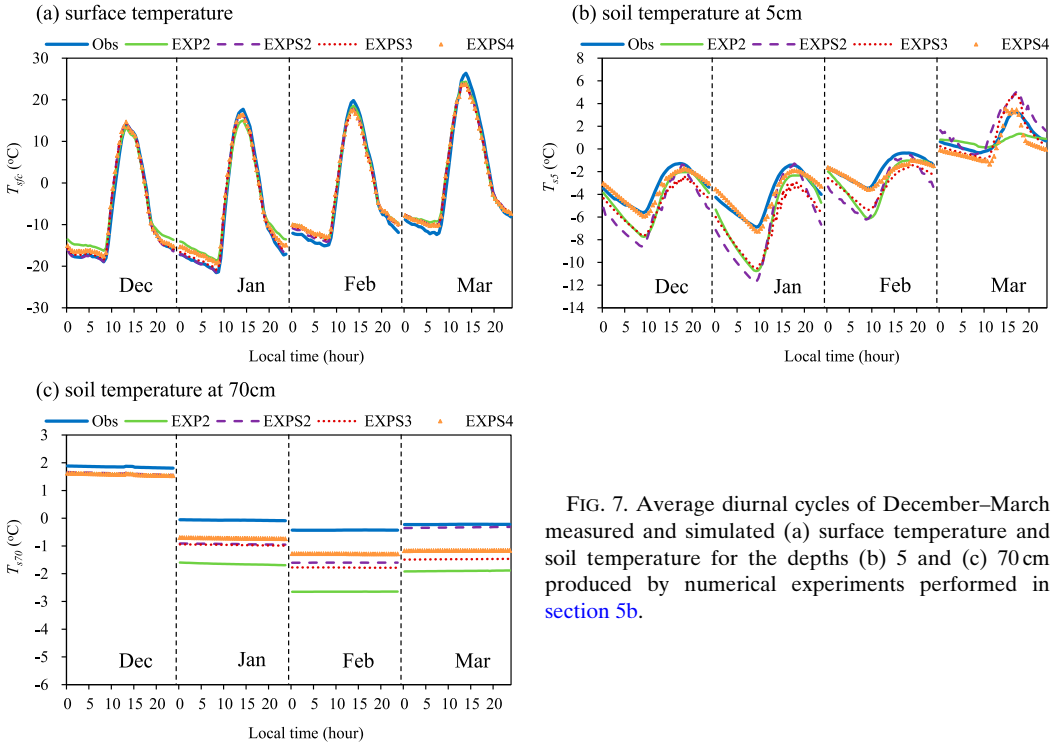

FIG. 7. Average diurnal cycles of December–March measured and simulated (a) surface temperature and soil temperature for the depths (b) 5 and (c) 70 cm produced by numerical experiments performed in section 5b.

depths of 5 and 70 cm produced with the three additional experiments. The results produced by the EXP2 are also shown for comparison purposes. Figure 8 shows further the time series of the measured and simulated liquid soil water profiles, and the corresponding RMSE statistics are added to Table 2. Again, it can be noted that the differences between the mean diurnal cycle of surface temperature simulated with these experiments are small (Fig. 7a).

In comparison to the EXP2 and EXPS1, the EXPS2 produces less latent energy during water phase change that leads to the increase in the amplitude of diurnal temperature variation at first soil layer (Fig. 7b) as well as the increase of temperature at deeper layer (Fig. 7c). The underestimation of nighttime temperature in the first soil layer noted for the EXP2 during soil freezing (December–February) is further degraded by the EXPS2, while the soil temperature in deeper layers is improved because of heat conduction from the surface to the deeper layers. Liquid soil water simulations are degraded by the EXPS2 (Fig. 8), and an RMSE increase is noted in Table 2 for the θ_{liq} simulations. After replacing the constant T_f with the one estimated by Eq. (11) as in EXPS3, the θ_{liq} simulations are improved (Fig. 8), and the corresponding RMSE statistics are reduced in comparison to the EXPS2 by about 33%, 46%, and 17% for depths of 5, 25, and 70 cm, respectively. Improvement is also noted in the simulation of the soil temperature at first layer (Table 1, Fig. 7b), although the overall temperatures across the soil profile are still underestimated.

The underestimation of the temperature in the soil profile is greatly improved by EXPS4 (Figs. 7b,c), which further implements the parameter ε representing the phase change efficiency. EXPS4 is able to capture the mean diurnal cycle of measured soil temperature in the first layer much better than other numerical experiments, and significant improvement is also achieved for the temperature simulation of deeper soil layers. Notably, the RMSE computed between the measured and simulated soil temperature for depths of 5, 25, and 70 cm is reduced by EXPS4 in comparison to EXPS3 about 48%, 55%, and 31%, respectively (Table 1). It can be thus inferred that the deficiency of the Noah LSM in simulating soil temperature may be related to the inappropriate treatment of phase change efficiency during soil freezing when less liquid water is present in the soil. EXPS4-simulated θ_{liq} dynamics are comparable to those produced by EXP2 and EXPS3 for the top two layers (Figs. 8a,b, Table 2), while the overestimation of θ_{liq} in a deeper layer (e.g., θ_{liq70}) noted for EXPS1 (Fig. 6c) is further amplified in EXPS4 (Fig. 8c) because the temperature is higher. It should be noted that both θ_{liq} and T_s measurements are collected at specific depths and then linearly interpolated to the midpoints of model soil layers, while the Noah simulations physically represent

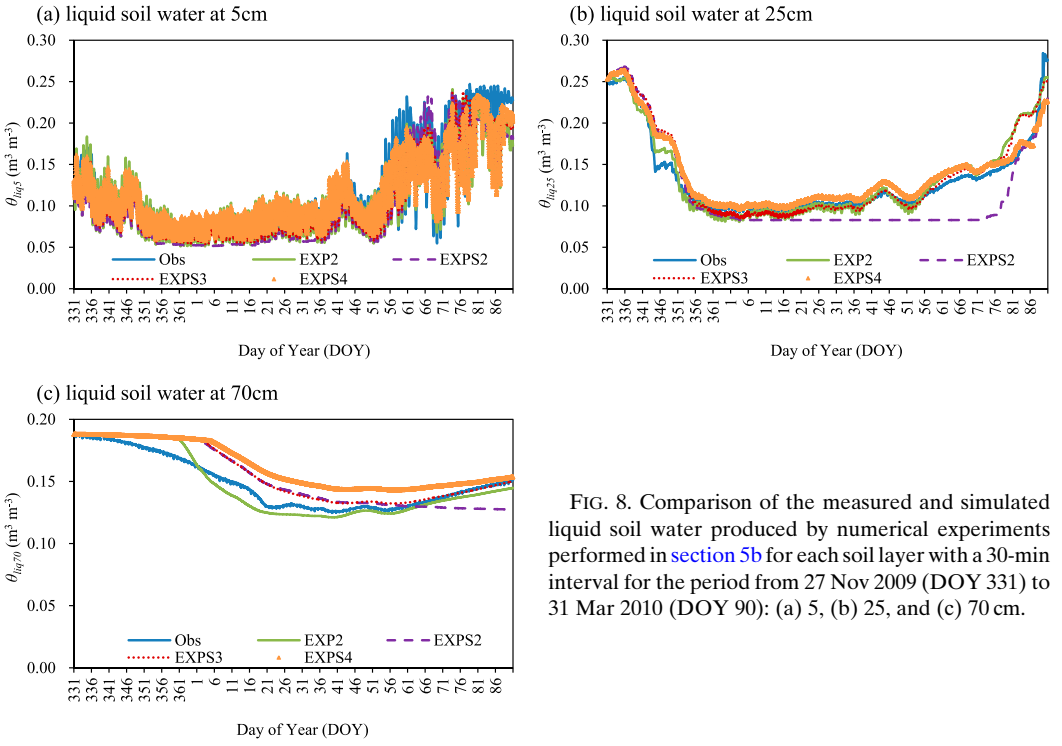

FIG. 8. Comparison of the measured and simulated liquid soil water produced by numerical experiments performed in section 5b for each soil layer with a 30-min interval for the period from 27 Nov 2009 (DOY 331) to 31 Mar 2010 (DOY 90): (a) 5, (b) 25, and (c) 70 cm.

the layer-averaged values. Specifically, the measured $\theta_{\text{liq}70}$ and T_{s70} are interpolated from measurements collected at 40- and 80-cm depths, and thus, the difference in freeze–thaw state of each depth may induce interpolation error since the maximum freezing depth is around 80 cm (see Fig. 7c). On the other hand, the simulated $\theta_{\text{liq}70}$ and T_{s70} represent the averaged values of the third model layer between 40 and 100 cm. The mismatch of the depths at which the measurements were taken and for the simulations are representative, and the interpolation may explain why the T_{s70} is better simulated by both EXPS1 and EXPS4, while the $\theta_{\text{liq}70}$ simulation is degraded in comparison to EXP2. Similar findings have also been reported in Xia et al. (2013).

6. Conclusions

In this paper, we investigate and improve the performance of the Noah LSM for simulating coupled water and heat flow in frozen soil over a Tibetan meadow ecosystem. A comprehensive dataset including in situ micrometeorological and soil moisture–temperature profile measurements has been collected for the period between 27 November 2009 and 31 March 2010, and analyses of the measurements reveal that the sensible heat flux H dominates the surface energy budget. It is also shown that the measured soil freezing characteristics are better captured by 1) modifying the parameter b_l that constrains the shape parameter of soil water retention curve to avoid the simulation of unrealistically high values for the liquid soil water content at very low temperature and 2) setting the parameter c_k that accounts for the effect of increase in specific surface of soil particles and ice–liquid water to zero.

Three numerical experiments are carried out to investigate the performance of Noah frozen soil parameterization with 1) its default model physics (Ctrl) and 2) implementation of augmentations (EXP1), including a diurnally varying roughness length for heat transfer z_{0h}, an asymptotic function for root water uptake, and vertical heterogeneous soil thermal and hydraulic properties. The third experiment (EXP2) further adopts the $c_k = 0$ and site-specific b_l values. The default Noah LSM (Ctrl) largely overestimates the daytime turbulent sensible and latent (LE) heat fluxes and underestimates the surface temperature T_{sfc}, which is greatly resolved by EXP1 with the implementation of the augmentations such as the scheme of diurnal thermal roughness length for heat transfer z_{0h} as also reported in Zheng et al. (2015b) for the warm monsoon season. In comparison to the Ctrl, the EXP1 reduces the RMSE computed between the measured and simulated H, LE, and T_{sfc} by about 36%, 17%, and 46%, respectively. Both Ctrl and EXP1 largely overestimate the liquid water contents θ_{liq} across the soil profile, which is significantly improved by EXP2 via further implementing $c_k = 0$ and site-specific

b_l values. The EXP2 reduces the RMSE in comparison to the Ctrl computed between the measured and simulated θ_{liq} for depths of 5, 25, and 70 cm by about 69%, 76%, and 53%, respectively. Further, it is found that all three experiments underestimate the temperature across the soil profile during soil freezing (December–February) because of the poor simulation of latent heat I_{lat} released or consumed during the phase change of soil water.

Four additional numerical experiments are conducted to investigate the sensitivity of model results to alternative treatments of thermal heat conductivity κ_h and I_{lat}. The results indicate that the overestimation of nighttime T_{sfc} by the Noah LSM is associated with the overestimation of κ_h values, and the underestimation of soil temperature profiles may be related to the inappropriate treatment of phase change efficiency that accounts for changing freezing rate with varying liquid water contents in the soil. The mismatching of represented depth between measurements and simulations as well as the interpolation error of measurements may explain why better soil temperature simulation at a deep layer followed with inappropriate θ_{liq} simulation. Additional work is, however, still needed to investigate other physical processes such as the vapor movement and its phase change as well as convective heat transport induced with water flow. A better understanding of the frozen soil processes over the Tibetan Plateau will inevitably enhance our ability to predict the impact of climatic change on the high-altitude ecosystems and regional hydrology.

Acknowledgments. This study was supported by funding from the Netherlands Organization for Scientific Research (Project ALW-GO/14-29), the National Natural Science Foundation of China (Grants 41405079 and 41530529), and the Key Research Program of the Chinese Academy of Sciences (Grant KZZD-EW-13). The measurements used in this study were provided by Zoige Plateau Wetland Ecosystem Research Station of CAREERI/CAS. For data access, please contact Jun Wen (jwen@lzb.ac.cn).

REFERENCES

Bao, H., T. Koike, K. Yang, L. Wang, M. Shrestha, and P. Lawford, 2016: Development of an enthalpy-based frozen soil model and its validation in a cold region in China. *J. Geophys. Res. Atmos.*, **121**, 5259–5280, doi:10.1002/2015JD024451.

Chen, F., and Coauthors, 1996: Modeling of land surface evaporation by four schemes and comparison with FIFE observations. *J. Geophys. Res.*, **101**, 7251–7268, doi:10.1029/95JD02165.

Chen, Y., K. Yang, D. Zhou, J. Qin, and X. Guo, 2010: Improving the Noah land surface model in arid regions with an appropriate parameterization of the thermal roughness length. *J. Hydrometeor.*, **11**, 995–1006, doi:10.1175/2010JHM1185.1.

Cheng, G., and T. Wu, 2007: Responses of permafrost to climate change and their environmental significance, Qinghai-Tibet Plateau. *J. Geophys. Res.*, **112**, F02S03, doi:10.1029/2006JF000631.

Cherkauer, K. A., and D. P. Lettenmaier, 1999: Hydrologic effects of frozen soils in the upper Mississippi River basin. *J. Geophys. Res.*, **104**, 19 599–19 610, doi:10.1029/1999JD900337.

Cosby, B. J., G. M. Hornberger, R. B. Clapp, and T. R. Ginn, 1984: A statistical exploration of the relationships of soil moisture characteristics to the physical properties of soils. *Water Resour. Res.*, **20**, 682–690, doi:10.1029/WR020i006p00682.

Cuo, L., Y. Zhang, T. J. Bohn, L. Zhao, J. Li, Q. Liu, and B. Zhou, 2015: Frozen soil degradation and its effects on surface hydrology in the northern Tibetan Plateau. *J. Geophys. Res. Atmos.*, **120**, 8276–8298, doi:10.1002/2015JD023193.

Dankers, R., E. J. Burke, and J. Price, 2011: Simulation of permafrost and seasonal thaw depth in the JULES land surface scheme. *Cryosphere*, **5**, 773–790, doi:10.5194/tc-5-773-2011.

Decharme, B., A. Boone, C. Delire, and J. Noilhan, 2011: Local evaluation of the Interaction between Soil Biosphere Atmosphere soil multilayer diffusion scheme using four pedotransfer functions. *J. Geophys. Res.*, **116**, D20126, doi:10.1029/2011JD016002.

Dente, L., Z. Vekerdy, J. Wen, and Z. Su, 2012: Maqu network for validation of satellite-derived soil moisture products. *Int. J. Appl. Earth Obs. Geoinf.*, **17**, 55–65, doi:10.1016/j.jag.2011.11.004.

Farouki, O. T., 1986: *Thermal Properties of Soils*. Series on Rock and Soil Mechanics, Vol. 11, Trans Tech, 136 pp.

Flerchinger, G. N., and K. E. Saxton, 1989: Simultaneous heat and water model of a freezing snow-residue-soil system I. Theory and development. *Trans. ASAE*, **32**, 565–571, doi:10.13031/2013.31040.

——, M. S. Seyfried, and S. P. Hardegree, 2006: Using soil freezing characteristics to model multi-season soil water dynamics. *Vadose Zone J.*, **5**, 1143–1153, doi:10.2136/vzj2006.0025.

Gouttevin, I., G. Krinner, P. Ciais, J. Polcher, and C. Legout, 2012: Multi-scale validation of a new soil freezing scheme for a land-surface model with physically-based hydrology. *Cryosphere*, **6**, 407–430, doi:10.5194/tc-6-407-2012.

Guo, D., and H. Wang, 2013: Simulation of permafrost and seasonally frozen ground conditions on the Tibetan Plateau, 1981–2010. *J. Geophys. Res. Atmos.*, **118**, 5216–5230, doi:10.1002/jgrd.50457.

Hansson, K., J. Šimůnek, M. Mizoguchi, L.-C. Lundin, and M. T. van Genuchten, 2004: Water flow and heat transport in frozen soil. *Vadose Zone J.*, **3**, 693–704, doi:10.2113/3.2.693.

Jin, H., R. He, G. Cheng, Q. Wu, S. Wang, L. Lü, and X. Chang, 2009: Changes in frozen ground in the source area of the Yellow River on the Qinghai-Tibet Plateau, China, and their eco-environmental impacts. *Environ. Res. Lett.*, **4**, 045206, doi:10.1088/1748-9326/4/4/045206.

Koren, V., J. Schaake, K. Mitchell, Q. Y. Duan, F. Chen, and J. M. Baker, 1999: A parameterization of snowpack and frozen ground intended for NCEP weather and climate models. *J. Geophys. Res.*, **104**, 19 569–19 585, doi:10.1029/1999JD900232.

Lawrence, D. M., and A. G. Slater, 2008: Incorporating organic soil into a global climate model. *Climate Dyn.*, **30**, 145–160, doi:10.1007/s00382-007-0278-1.

——, ——, V. E. Romanovsky, and D. J. Nicolsky, 2008: Sensitivity of a model projection of near-surface permafrost degradation to soil column depth and representation of soil organic matter. *J. Geophys. Res.*, **113**, F02011, doi:10.1029/2007JF000883.

Letts, M. G., N. T. Roulet, N. T. Comer, M. R. Skarupa, and D. L. Verseghy, 2000: Parametrization of peatland hydraulic properties for the Canadian land surface scheme. *Atmos.–Ocean*, **38**, 141–160, doi:10.1080/07055900.2000.9649643.

Li, Q., S. Sun, and Y. Xue, 2010: Analyses and development of a hierarchy of frozen soil models for cold region study. *J. Geophys. Res.*, **115**, D03107, doi:10.1029/2009JD012530.

Li, X., R. Jin, X. Pan, T. Zhang, and J. Guo, 2012: Changes in the near-surface soil freeze–thaw cycle on the Qinghai-Tibetan Plateau. *Int. J. Appl. Earth Obs. Geoinf.*, **17**, 33–42, doi:10.1016/j.jag.2011.12.002.

Lundin, L.-C., 1990: Hydraulic properties in an operational model of frozen soil. *J. Hydrol.*, **118**, 289–310, doi:10.1016/0022-1694(90)90264-X.

Luo, L., and Coauthors, 2003: Effects of frozen soil on soil temperature, spring infiltration, and runoff: Results from the PILPS 2(d) experiment at Valdai, Russia. *J. Hydrometeor.*, **4**, 334–351, doi:10.1175/1525-7541(2003)4<334:EOFSOS>2.0.CO;2.

Masson, V., and Coauthors, 2013: The SURFEXv7.2 land and ocean surface platform for coupled or offline simulation of Earth surface variables and fluxes. *Geosci. Model Dev.*, **6**, 929–960, doi:10.5194/gmd-6-929-2013.

Niu, G.-Y., and Z.-L. Yang, 2006: Effects of frozen soil on snowmelt runoff and soil water storage at a continental scale. *J. Hydrometeor.*, **7**, 937–952, doi:10.1175/JHM538.1.

——, and Coauthors, 2011: The community Noah land surface model with multiparameterization options (Noah-MP): 1. Model description and evaluation with local-scale measurements. *J. Geophys. Res.*, **116**, D12109, doi:10.1029/2010JD015139.

Oleson, K., and Coauthors, 2013: Technical description of version 4.5 of the Community Land Model (CLM). NCAR Tech. Note NCAR/TN-503+STR, 420 pp., doi:10.5065/D6RR1W7M.

Peters-Lidard, C. D., E. Blackburn, X. Liang, and E. F. Wood, 1998: The effect of soil thermal conductivity parameterization on surface energy fluxes and temperatures. *J. Atmos. Sci.*, **55**, 1209–1224, doi:10.1175/1520-0469(1998)055<1209:TEOSTC>2.0.CO;2.

Poutou, E., G. Krinner, C. Genthon, and N. de Noblet-Ducoudré, 2004: Role of soil freezing in future boreal climate change. *Climate Dyn.*, **23**, 621–639, doi:10.1007/s00382-004-0459-0.

Salama, M. S., R. Van der Velde, L. Zhong, Y. Ma, M. Ofwono, and Z. Su, 2012: Decadal variations of land surface temperature anomalies observed over the Tibetan Plateau by the Special Sensor Microwave Imager (SSM/I) from 1987 to 2008. *Climatic Change*, **114**, 769–781, doi:10.1007/s10584-012-0427-3.

Slater, A. G., T. J. Bohn, J. L. McCreight, M. C. Serreze, and D. P. Lettenmaier, 2007: A multimodel simulation of pan-Arctic hydrology. *J. Geophys. Res.*, **112**, G04S45, doi:10.1029/2006JG000303.

Stevens, M. B., J. E. Smerdon, J. F. González-Rouco, M. Stieglitz, and H. Beltrami, 2007: Effects of bottom boundary placement on subsurface heat storage: Implications for climate model simulations. *Geophys. Res. Lett.*, **34**, L02702, doi:10.1029/2006GL028546.

Su, Z., P. de Rosnay, J. Wen, L. Wang, and Y. Zeng, 2013: Evaluation of ECMWF's soil moisture analyses using observations on the Tibetan Plateau. *J. Geophys. Res. Atmos.*, **118**, 5304–5318, doi:10.1002/jgrd.50468.

van der Velde, R., M. S. Salama, T. Pellarin, M. Ofwono, Y. Ma, and Z. Su, 2014: Long term soil moisture mapping over the Tibetan plateau using Special Sensor Microwave/Imager. *Hydrol. Earth Syst. Sci.*, **18**, 1323–1337, doi:10.5194/hess-18-1323-2014.

Viterbo, P., A. Beljaars, J.-F. Mahfouf, and J. Teixeira, 1999: The representation of soil moisture freezing and its impact on the stable boundary layer. *Quart. J. Roy. Meteor. Soc.*, **125**, 2401–2426, doi:10.1002/qj.49712555904.

Wang, G., G. Liu, and C. Li, 2012: Effects of changes in alpine grassland vegetation cover on hillslope hydrological processes in a permafrost watershed. *J. Hydrol.*, **444–445**, 22–33, doi:10.1016/j.jhydrol.2012.03.033.

Wu, Q., and T. Zhang, 2010: Changes in active layer thickness over the Qinghai-Tibetan Plateau from 1995 to 2007. *J. Geophys. Res.*, **115**, D09107, doi:10.1029/2009JD012974.

Wu, T., L. Zhao, R. Li, Q. Wang, C. Xie, and Q. Pang, 2013: Recent ground surface warming and its effects on permafrost on the central Qinghai-Tibet Plateau. *Int. J. Climatol.*, **33**, 920–930, doi:10.1002/joc.3479.

Xia, Y., and Coauthors, 2013: Validation of Noah-simulated soil temperature in the North American Land Data Assimilation System phase 2. *J. Appl. Meteor. Climatol.*, **52**, 455–471, doi:10.1175/JAMC-D-12-033.1.

Yang, K., Y. Y. Chen, and J. Qin, 2009: Some practical notes on the land surface modeling in the Tibetan Plateau. *Hydrol. Earth Syst. Sci.*, **13**, 687–701, doi:10.5194/hess-13-687-2009.

Zeiliguer, A. M., Y. A. Pachepsky, and W. J. Rawls, 2000: Estimating water retention of sandy soils using the additivity hypothesis. *Soil Sci.*, **165**, 373–383, doi:10.1097/00010694-200005000-00001.

Zeng, X., Z. Wang, and A. Wang, 2012: Surface skin temperature and the interplay between sensible and ground heat fluxes over arid regions. *J. Hydrometeor.*, **13**, 1359–1370, doi:10.1175/JHM-D-11-0117.1.

Zhang, T., R. G. Barry, K. Knowles, J. A. Heginbottom, and J. Brown, 1999: Statistics and characteristics of permafrost and ground-ice distribution in the Northern Hemisphere. *Polar Geogr.*, **23**, 132–154, doi:10.1080/10889379909377670.

——, ——, ——, F. Ling, and R. Armstrong, 2003: Distribution of seasonally and perennially frozen ground in the Northern Hemisphere. *Permafrost*, M. Phillips, S. M. Springman, and L. U. Arenson, Eds., A. A. Balkema, 1289–1294.

Zhang, X., S. F. Sun, and Y. Xue, 2007: Development and testing of a frozen soil parameterization for cold region studies. *J. Hydrometeor.*, **8**, 690–701, doi:10.1175/JHM605.1.

Zhang, Y., S. K. Carey, and W. L. Quinton, 2008: Evaluation of the algorithms and parameterizations for ground thawing and freezing simulation in permafrost regions. *J. Geophys. Res.*, **113**, D17116, doi:10.1029/2007JD009343.

——, ——, ——, J. R. Janowicz, J. W. Pomeroy, and G. N. Flerchinger, 2010: Comparison of algorithms and parameterisations for infiltration into organic-covered permafrost soils. *Hydrol. Earth Syst. Sci.*, **14**, 729–750, doi:10.5194/hess-14-729-2010.

Zhao, L., D. M. Gray, and D. H. Male, 1997: Numerical analysis of simultaneous heat and mass transfer during infiltration into frozen ground. *J. Hydrol.*, **200**, 345–363, doi:10.1016/S0022-1694(97)00028-0.

Zheng, D., R. van der Velde, Z. Su, M. J. Booij, A. Y. Hoekstra, and J. Wen, 2014: Assessment of roughness length schemes implemented within the Noah land surface model for high-altitude regions. *J. Hydrometeor.*, **15**, 921–937, doi:10.1175/JHM-D-13-0102.1.

——, ——, ——, X. Wang, J. Wen, M. J. Booij, A. Y. Hoekstra, and Y. Chen, 2015a: Augmentations to the Noah model physics for application to the Yellow River source area. Part I: Soil water flow. *J. Hydrometeor.*, **16**, 2659–2676, doi:10.1175/JHM-D-14-0198.1.

——, ——, ——, ——, ——, ——, ——, and ——, 2015b: Augmentations to the Noah model physics for application to the Yellow River source area. Part II: Turbulent heat fluxes and soil heat transport. *J. Hydrometeor.*, **16**, 2677–2694, doi:10.1175/JHM-D-14-0199.1.

——, ——, ——, J. Wen, M. J. Booij, A. Y. Hoekstra, and X. Wang, 2015c: Under-canopy turbulence and root water uptake of a Tibetan meadow ecosystem modeled by Noah-MP. *Water Resour. Res.*, **51**, 5735–5755, doi:10.1002/2015WR017115.

——, and Coauthors, 2016: Impacts of Noah model physics on catchment-scale runoff simulations. *J. Geophys. Res. Atmos.*, **121**, 807–832, doi:10.1002/2015JD023695.

——, R. Van Der Velde, Z. Su, J. Wen, and X. Wang, 2017: Assessment of Noah land surface model with various runoff parameterizations over a Tibetan river. *J. Geophys. Res. Atmos.*, **122**, 1488–1504, doi:10.1002/2016JD025572.